Journal of
Materials Chemistry A

ROYAL SOCIETY
OF CHEMISTRY

PAPER

View Article Online
View Journal | View Issue

Check for updates

Cite this: J. Mater. Chem. A, 2025, 13, 36151

In situ generation of the spinel structured $FeCr_2O_4$ catalyst for CO_2-assisted ethane oxidative dehydrogenation

Meng Du,[abc] Bing Nan,*[ab] Yunan Li,[ac] Zhengwu Liu,[ac] Kunming Hou,[b] Yulin Qin,[b] Guanhaojie Zheng,[b] Zhenye Liang,[ac] Lina Zhang,[b] Daolei Wang,[d] Lingling Guo,[b] Luozhen Jiang,[b] Chen Tian,[b] Peng Fan,[b] Nannan Sun*[b] and Lina Li*[ab]

Received 24th June 2025
Accepted 13th September 2025

DOI: 10.1039/d5ta05111h

rsc.li/materials-a

Ethylene (C_2H_4) is a crucial raw material for the chemical industry. Recently, the oxidative dehydrogenation of ethane (C_2H_6) using CO_2 as a milder oxidant (CO_2-ODHE) has been proposed as a potential method for C_2H_4 production through the efficient utilization of shale gas and the mitigation of CO_2 emissions. In this work, a series of Fe, Cr–Fe, and Cr oxides were prepared by a two-step urea precipitation method with Fe_3O_4, $FeCr_2O_4$, and Cr_2O_3 components, in which the Cr–Fe catalyst exhibits better activity with the conversion of ethane (35%) and CO_2 (27%) and stable C_2H_4 yield (18%) at 650 °C. Through TEM, SEM, Raman, XAFS and *in situ* XRD results, it was found that the *in situ* formation of $FeCr_2O_4$ during the CO_2-ODHE reaction can enhance the thermostability of the Cr–Fe catalyst. Furthermore, the generated $FeCr_2O_4$ effectively adsorbs and activates CO_2 molecules to reduce the generation of deposited carbon on the surface of the Cr–Fe catalyst.

1. Introduction

Ethylene (C_2H_4) is recognized as the cornerstone of the petrochemical industry, serving as a crucial intermediate for over 70% of fundamental organic chemical raw materials, including ethylene oxide, polypropylene, and polystyrene, which are widely applied in textiles, plastics, and other fields.[1,2] With the recent continuous increase in verified shale gas reserves, the catalytic dehydrogenation of light alkanes, which constitute more than 20% of shale gas, has emerged as a promising and economically efficient pathway for ethylene production.[3,4] The oxidative dehydrogenation of ethane using CO_2 (CO_2-ODHE) refers to the process with CO_2 as a mild oxidant to produce ethylene with lower energy consumption and a higher reaction equilibrium constant[5] and eliminate carbon deposition[6] by providing reactive oxygen species (*O). CO_2 can react with coke deposited on the catalyst surface *via* the Boudouard reaction ($CO_2 + C = 2CO$), thus improving catalyst performance. Furthermore, taking into account both thermodynamic and kinetic factors, the CO_2-ODHE process needs to be conducted at high temperatures (>873 K), which results in several problems such as poor thermal stability, susceptibility to sintering,[7] and carbon deposition, hindering its industrial applications.[8] However, the sintering of the active species at high reaction temperatures can lead to irreversible deactivation of the catalysts.[9] In addition, the side reactions, such as the reforming reaction and the reverse water–gas shift (RWGS) reaction, can significantly influence the overall catalytic performance. The reforming reaction with the conversion of alkanes into syngas (CO and H_2) competes with the desired dehydrogenation pathway, leading to reduced ethylene selectivity and yield.[10] On the other hand, the RWGS reaction ($CO_2 + H_2 \leftrightarrow CO + H_2O$) can promote the reaction equilibrium by consuming H_2.[5] Therefore, developing efficient catalysts with excellent catalytic performance, sintering resistance, and anti-coking properties for the CO_2-ODHE reaction has received wide research attention for both academic and practical significance.

Recently, a series of typical non-noble metal CO_2-ODHE catalysts have been widely developed, such as Cr-, Ga-, and Fe-based oxides.[5,11–15] Chromium-based catalysts are the most widely studied active components in this field in the CO_2-ODHE reaction because of their high activity and selectivity, which can make a recycle between metallic and oxidized Cr species to adsorb and activate CO_2 for the dehydrogenation of C_2H_6.[16] Both the inevitable toxicity of Cr^{6+} and the easy aggregation of Cr_2O_3 further restrict the application of Cr-based catalysts in the CO_2-ODHE reaction.[17] In addition, Fe, as a typical promoter, is frequently used to modify active metals (Cr, Co, or Ni) by altering electronic and coordination structures. Yan *et al.*[18]

---

[a] *Shanghai Institute of Applied Physics, Chinese Academy of Sciences, Shanghai 201204, China. E-mail: lilina@sinap.ac.cn*

[b] *Shanghai Advanced Research Institute, Chinese Academy of Sciences, Shanghai 201210, China. E-mail: sunnn@sari.ac.cn; nanb@sari.ac.cn*

[c] *University of Chinese Academy of Sciences, Beijing 100049, China*

[d] *Division of China, TILON Group Technology Limited, Shanghai, China*

found that the Ni–FeO_x interface sites can selectively break C–H rather than C–C bonds in C_2H_6 to promote the formation of C_2H_4. Furthermore, the Fe^{3+}/Fe^{2+} redox cycle and unique α-Fe component can also effectively prevent reforming reactions.[19] Recently, $FeCr_2O_4$ with a unique spinel structure has received wide attention because of its good conductivity, reducibility, and thermodynamic stability, and has been evidenced as an excellent participant in high-temperature reactions.[9,20] Besides, according to kinetic experimental and DFT studies, $FeCr_2O_4$ could activate the sp^2 C–H bond of benzene with a lower activation energy compared to the Cr_2O_3 component.[21] Bogdan *et al.* studied carbon-supported Fe–Cr–Ni and Fe–Cr oxide catalysts, discovering that the formation of the $FeCr_2O_4$ phase on the surface of Fe–Cr/C catalysts is responsible for the high stability and high ethylene selectivity at 700 °C.[22–24] And in another study, they found that the formation of $FeCr_2O_4$ could prevent the reduction of iron and the formation of iron carbides.[25] Additionally, in their latest research, it was found that a reversible water–gas shift reaction is activated by spinel-type oxide phases, which was characterized in detail by *in situ* magnetometry and Mössbauer spectroscopy methods.[26] While these studies highlight the beneficial role of the supported $FeCr_2O_4$ phase, the potential for its *in situ* generation during the demanding CO_2-ODHE reaction itself, and its subsequent impact on catalytic performance and stability, remain less explored. Thus, we investigate the structural evolution of FeCr oxide catalysts under CO_2-ODHE conditions, specifically focusing on whether the beneficial $FeCr_2O_4$ spinel phase forms *in situ* during the reaction and how this dynamic process governs catalytic behavior.

Here, we synthesized nano-iron oxide, chromium oxide, and FeCr bimetallic oxides using a two-step urea precipitation method and applied them in the CO_2-ODHE reaction. Through a series of structural characterization studies such as XRD, SEM, TEM, Raman, XAFS, and temperature-programmed experiments, we found that the spinel structured $FeCr_2O_4$, which is formed *in situ* under the reaction atmosphere, exhibited good thermal stability to endure the high reaction temperature. Meanwhile, $FeCr_2O_4$ could enhance the adsorption and activation of CO_2 to mitigate coke accumulation and improve the activity.

2. Experimental

2.1. Catalyst preparation

Without any additional purification, all of the chemicals utilized in this work were of analytical grade and bought from Sinopharm Chemical Reagent Co., Ltd.

The catalysts used in this study were synthesized using a two-step urea hydrolysis co-precipitation method. Ferric nitrate ($Fe(NO_3)_3 \cdot 9H_2O$) and chromium nitrate ($Cr(NO_3)_3 \cdot 9H_2O$) were chosen as the metal precursors. The metal ion ratios were controlled at 1 : 0, 1 : 3, and 0 : 1, respectively. The metal nitrates were mixed, stirred, and dissolved in deionized water. The mixture was aged for 1 h and then transferred to a 100 mL polytetrafluoroethylene (PTFE)-lined autoclave. The autoclave was first maintained at 80 °C in an oven for 6 h and then heated to 180 °C for 24 h. Afterward, the autoclave was allowed to cool naturally to room temperature. The resulting precipitates were collected by multiple centrifugations and washed with deionized water until the pH reached 7. The final products were dried in a vacuum oven at 70 °C and then calcined at 400 °C for 4 h with a heating rate of 10 °C min^{-1}. The fresh samples obtained were designated as Fe, Cr–Fe, and Cr, respectively.

2.2. Characterization

The nitrogen adsorption–desorption isotherm was recorded on an ASAP2020-HD88 analyzer (Micromeritics Co., Ltd.) at 77 K. Before introducing N_2, the measured powders were degassed at 250 °C for 4 h under vacuum (<100 μm Hg). The pore-size distribution of each sample was calculated using the BJH method in accordance with the desorption branch of the obtained isotherms. The BET specific surface areas were calculated from data in the relative pressure range between 0.06 and 0.30.

The powder X-ray diffraction (XRD) patterns were obtained using Cu $K_{\alpha 1}$ radiation ($\lambda = 1.540598$ Å) with a scanning range of 10°–90° on a Panalytical Empyrean X-ray diffractometer (40 kV and 40 mA). Prior to each test, the ground sample was planished on a quartz sample holder.

The transmission electron microscopy (TEM), high-resolution transmission electron microscopy (HRTEM) and scanning transmission electron microscopy-energy dispersive spectrometry (STEM-EDS) elemental mapping images were recorded on an FEI TALOS F200X microscope with an acceleration voltage of 200 kV. The measured samples were first ultrasonically dispersed in pure alcohol for about 5 min, and then a drop of the liquid supernatant was applied to a very thin carbon film. Before being placed inside the sample holder, the sample grid was allowed to dry naturally. The scanning electron microscope (SEM) images were obtained from a field emission scanning electron microscope (Zeiss, Sigma 500).

X-ray photoelectron spectroscopy (XPS) for the used samples was performed by using a PHI 5000 Versa Probe III with a monochromatic Al Kα X-ray source with a beam size of 100 μm × 1400 μm. Charge compensation was achieved by dual beam charge neutralization and the binding energy was corrected by setting the binding energy of the hydrocarbon C 1s feature to 284.8 eV.

The Raman spectra were collected using a Renishaw Raman InVia reflex microscope with laser excitation at 532 nm. The samples were attached to a glass slide, and Raman shifts were acquired from 100 to 1900 cm^{-1} with a spectral resolution of 1 cm^{-1}. For each experimental run, the scanning parameter for each Raman spectrum was set at 100 s in order to improve the signal-to-noise ratio. In order to assess the repeatability of the spectral results, several spot analyses were performed on various regions of the same sample.

The X-ray absorption fine structure (XAFS) spectra at the Fe K-edge ($E^0 = 7112$ eV) and Cr K-edge ($E^0 = 5989$ eV) were recorded at BL14W1 and 16U1 beam lines of Shanghai Synchrotron Radiation Facility (SSRF) operated at 3.5 GeV in "top-up" mode with a constant current of 220 mA. The XAFS data were recorded in transmission mode. The energy was calibrated according to the absorption edge of pure Fe and Cr foil. The data were analyzed using the Demeter software package.[27] For the X-ray absorption near edge structure (XANES) part, the experimental absorption coefficients as a function of energies $\mu(E)$ were processed by background subtraction and normalization procedures, and reported as "normalized absorption". The chemical valence of Fe was determined with the linear combination fit by comparison to the corresponding references of Fe/Fe_3O_4 based on the normalized XANES profiles in the Athena software. For the extended X-ray absorption fine structure (EXAFS) part, the Fourier transformed (FT) data in R space were analyzed by multiple Fe compound models for Fe–O, Fe–O–Fe or Fe–O–Cr shells, respectively. The passive electron factors, $S_0{}^2$, were determined by fitting the experimental Fe foil data and fixing the Fe–Fe coordination number (CN) to be 8 + 6, and then fixed for further analysis of the measured samples. For Cr, the Fourier transform (FT) in R-space is analyzed by applying Cr_2O_3 and Cr_2FeO_4 models to Cr–O and Cr–O–Cr, respectively. Similarly, amp was obtained by fixing the coordination number (CN) of Cr–Cr as 6 according to the data of Cr foil, and then $S_0{}^2$ was fixed to further analyze the measured samples. The parameters describing the electronic properties (*e.g.*, correction to the photoelectron energy origin, E^0) and local structure environment including the coordination number (CN), bond distance (R) and Debye–Waller (D.W.) factor around the absorbing atoms were allowed to vary during the fitting process. The fitted ranges for k were selected to be k = 3.0–12.0 Å^{-1} and 2.8–11.0 Å^{-1} (k^3 weighted) for Fe and Cr samples, respectively. The Fourier transformed (FT) data in R space were analyzed by selecting R = 1.0–3.4 and 1.2–3.0 Å (k^3 weighted), respectively.

In situ X-ray diffraction (XRD) measurements of Cr–Fe catalysts were carried out within a compact flow cell at the BL02U2 beam line of Shanghai Synchrotron Radiation Facility (SSRF) (λ = 0.79743 Å). Two-dimensional XRD data were acquired by using a Pilatus 2M with a distance of *c.a.* 240 mm from the samples. The catalyst sample was compressed into a disc with a diameter of 10 mm and then placed on the heating stage of the *in situ* cell. It was reduced *in situ* by a mixture of H_2/Ar (20/20 mL min^{-1}) with the temperature ramping from room temperature to 450 °C (40 °C min^{-1}) and holding for 30 min. After flushing in Ar for 10 min, the catalyst was sequentially exposed to the reaction gases (CO_2/C_2H_6/Ar = 10/10/20 mL min^{-1}), and then the temperature was increased to 500, 600, 650, and 700 °C (10 °C min^{-1}), respectively. Each temperature point was maintained for 15 min. The two-dimensional (2D) diffraction images were continuously collected by using a Pilatus3 S-2M detector. The LaB_6 standard was used for wavelength calibration. The 2D images were subsequently integrated using the program Dioptas to obtain XRD profiles. The 2θ angle was converted to the corresponding value of the Cu $K_{\alpha1}$ radiation (λ = 1.54056 Å).

The temperature-programmed reduction by hydrogen (H_2-TPR) measurements for the catalyst samples were conducted on a Micromeritics AutoChem II 2920 instrument equipped with a thermal conductivity detector (TCD). After being pretreated under O_2 (5% O_2/He) flow in a quartz U-tube reactor at 300 °C for 30 min, the samples (50 mg) were cooled down to room temperature in Ar. Then 5% H_2/Ar (50 mL min^{-1}) was introduced to pass through the catalyst bed until a stable TCD signal was observed. Subsequently, a temperature ramping program from room temperature to 800 °C at the rate of 10 °C min^{-1} was performed.

CO_2-temperature programmed desorption (CO_2-TPD) was carried out on an AutoChem II 2920 (Micromeritics, USA) instrument and a mass spectrometer (LC-D200M, TILON) was used to gather gas signals. 100 mg of fresh catalyst was placed in a U-shaped quartz sample tube. Prior to TPD studies, the catalyst sample was processed with 5% H_2/Ar (50 mL min^{-1}) at 450 °C for 90 min and then cooled down to room temperature using the same steam. He was purged for 30 min and then the catalyst was exposed to 5% CO_2/He (50 mL min^{-1}) for 1 h until surface saturation was achieved. The weakly physisorbed CO_2 was purged by flushing in He (50 mL min^{-1}) for 30 min. Finally, desorption of CO_2 was carried out by increasing the temperature to 700 °C at a ramp of 10 °C min^{-1} under He. The signals of He ($m/z = 4$) and CO_2 ($m/z = 44$) were detected by using the mass spectrometer during the investigation.

CO_2-temperature programed surface reaction (CO_2-TPSR) experiments were performed to prove the oxidation of deposited carbon by CO_2 for used catalysts (85 mg) on a similar instrument to CO_2-TPD. After being pretreated under He (30 mL min^{-1}) in a quartz U-tube reactor at 150 °C for 30 min, the samples were cooled down to room temperature in He. Then 5% CO_2/He (30 mL min^{-1}) was introduced to pass through the catalyst bed until a stable TCD signal was observed. Subsequently, a temperature ramping program from room temperature to 900 °C at a rate of 10 °C min^{-1} was performed under 5% CO_2/He flow. The signals of He ($m/z = 4$) and CO_2 ($m/z = 44$) were detected by using the mass spectrometer during the investigation. He-TPSR experiments were conducted to prove the intrinsic active oxygen species for coke elimination of the used catalysts (50 mg), following the same procedure as the CO_2-TPSR experiments, with the only difference being that the CO_2 flow was replaced by a He flow.

The TPO experiment was performed using a thermoanalyzer (Setaram Labsys Evo 1150) coupled with a mass spectrometer for evolved gas analysis to quantify the amount of coke deposited on the used catalysts after CO_2-ODHE at 700 °C. The ~10 mg catalyst was placed in a 70 μL alumina crucible and heated at 40–800 °C (5 °C min^{-1}) under 20% O_2/N_2 flow (40 mL min^{-1}). The amount of CO_2 in the outlet gas was quantified by using an online mass spectrometer.

2.3. Catalytic tests

The catalytic performance of the samples in CO_2-ODHE was evaluated in a 6 mm fixed-bed micro-reactor. 100 mg of catalyst was used in each test. The catalyst was fixed in the middle of the bed with quartz cotton, and the reaction temperature of the catalyst was monitored by a thermocouple located in the center of the bed. Before the catalytic performance test, the catalysts were pretreated at 450 °C in a 50% H_2/Ar flow for 1 hour, and then the reaction was initiated by feeding a mixture gas with C_2H_6/CO_2/Ar = 10 : 10 : 20 mL min^{-1} under atmospheric pressure, with N_2 being used as the internal standard. The reaction temperature ranged from 500 to 700 °C, with a step increment of 50 °C. Each temperature point was maintained for 40 min to ensure the reliability and repeatability of the gas chromatography data, allowing us to obtain activity data for the catalysts at different temperatures. The samples after the reaction were designated as Fe-used, Cr–Fe-used, and Cr-used, respectively.

The reaction products were analyzed by using a gas chromatograph (Agilent Technologies 7890B), using a flame ionization detector (FID) equipped with an alumina capillary column to detect CH_4, C_2H_6, and C_2H_4 (N_2 carrier gas) and a thermal conductivity detector (TCD) packed with Porapak Q columns, N columns and molecular sieve 5 A columns to detect H_2, N_2, CO, CH_4, and CO_2 (He carrier gas). C_2H_6 conversion ($X(C_2H_6)$), CO_2 conversion ($X(CO_2)$), C_2H_4 yield ($Y(C_2H_4)$), C_2H_4 selectivity ($S(C_2H_4)$), CO selectivity ($S(CO)$) and CH_4 selectivity ($S(CH_4)$) in gaseous products and carbon balance are calculated as follows:

$$X(C_2H_6) = [F(C_2H_6,\text{ in}) - F(C_2H_6,\text{ out})]/F(C_2H_6,\text{ in}) \times 100\%,$$

$$X(CO_2) = [F(CO_2,\text{ in}) - F(CO_2,\text{ out})]/F(CO_2,\text{ in}) \times 100\%,$$

$$Y(C_2H_4) = F(C_2H_4,\text{ out})/F(C_2H_6,\text{ in}) \times 100\%,$$

$$S(C_2H_4) = Y(C_2H_4)/X(C_2H_6) \times 100\%,$$

$$S_{\text{gas}}(C_2H_4) = 2 \times F(C_2H_4,\text{ out})/[2 \times F(C_2H_4,\text{ out}) + F(CO,\text{ out}) + F(CH_4,\text{ out})] \times 100\%,$$

$$S_{\text{gas}}(CH_4) = F(CH_4,\text{ out})/[2 \times F(C_2H_4,\text{ out}) + F(CO,\text{ out}) + F(CH_4,\text{ out})] \times 100\%,$$

$$S_{\text{gas}}(CO) = F(CO,\text{ out})/[2 \times F(C_2H_4,\text{ out}) + F(CO,\text{ out}) + F(CH_4,\text{ out})] \times 100\%,$$

$$\text{Carbon balance} = [2 \times F(C_2H_6,\text{ out}) + 2 \times F(C_2H_4,\text{ out}) + F(CH_4,\text{ out}) + F(CO_2,\text{ out}) + F(CO,\text{ out})]/[2 \times F(C_2H_6,\text{ in}) + F(CO_2,\text{ in})] \times 100\%,$$

where $F(i,\text{ in})$ and $F(i,\text{ out})$ stand for the volume flow of component i (mL min^{-1}) after N_2 correction at the inlet and outlet, respectively.

$$F(i) = F(N_2) \times A(i)/A(N_2) \times R(i)/R(N_2)$$

where$A(i)$ is the peak area of component i in the gas chromatogram and $R(i)$ is the relative response factor of component i (determined by calibration with standard gases).

In the comparison of ethylene formation rates, the effects of space velocity and inert gas dilution have been excluded using the following calculation formula:

$$\text{Rates of ethylene formation } (\mu\text{mol } g_{\text{cat}}^{-1}\text{ s}^{-1}) = Y(C_2H_4) \times \text{space velocity (GHSV)} \times (V_{C_2H_6}/V_{\text{total}})/V_{\text{m}}$$

3. Results and discussion

3.1. CO_2-ODHE catalytic reaction performance

In this work, a series of monometallic and bimetallic iron–chromium oxide catalysts were evaluated by a CO_2-assisted ethane dehydrogenation reaction. Typically, the catalytic performance of samples with different Cr/Fe ratios was tested to optimize the catalyst (Fig. S1). The Cr–Fe (3 : 1) sample with the highest ethylene yield was selected for comparison with monometallic samples to investigate the structure–activity relationship.

During the CO_2-ODHE, C_2H_4, CH_4, CO, H_2, H_2O, and C products are formed according to the following reactions:[18,28,29]

$$\text{The } CO_2 \text{ dehydrogenation of ethane to ethylene: } C_2H_6 + CO_2 \leftrightarrow C_2H_4 + CO + H_2O \quad (1)$$

$$\text{The direct dehydrogenation of ethane (DHE): } C_2H_6 \leftrightarrow C_2H_4 + H_2 \quad (2)$$

$$\text{The reverse water–gas shift reaction (RWGS): } CO_2 + H_2 \leftrightarrow CO + H_2O \quad (3)$$

$$\text{The Boudouard reaction: } CO_2 + C \leftrightarrow 2CO \quad (4)$$

$$\text{The dry reforming reaction (DRE): } C_2H_6 + 2CO_2 \leftrightarrow 4CO + 3H_2 \quad (5)$$

$$\text{The } C_2H_6 \text{ cracking reaction: } C_2H_6 + H_2 \rightarrow 2CH_4 \quad (6)$$

$$\text{Coke formation: } C_2H_6 \leftrightarrow 2C + 3H_2 \quad (7)$$

The main and side reactions collectively determine the overall material balance and reaction activity. The results of catalytic experiments and the mass ratio of products at 650 °C are shown in Fig. 1 and Table S1. As the temperature increased, the Cr–Fe bimetallic sample exhibited much better activity compared with the monometallic Fe and Cr samples. At 650 °C, the conversion of ethane and CO_2 approached 35% and 27%, respectively. The product mass content, with CO constituting 61% and ethylene accounting for 23%, while coke formation representing only 5%, indicates that the Cr–Fe sample is a promising catalyst for the ethane oxidative dehydrogenation reaction. Although the monometallic Cr catalyst exhibited 20% for ethane conversion at 650 °C, consistent with unsupported Cr-based catalysts even at a lower space velocity of 3600 mL g_{cat}^{-1} h^{-1},[7,12] both the CO_2 conversion and ethylene yield were significantly lower compared to the Cr–Fe catalyst. Additionally, the significant amount of coke deposited on the monometallic Cr catalyst (accounting for 66% of the mass content) clearly indicates the rapid occurrence of coke formation under high-temperature conditions. Meanwhile, the monometallic Fe catalyst exhibited poor catalytic performance in the CO_2-ODHE reaction, only achieving the conversion of both C_2H_6 and CO_2 below 5%, which demonstrated the poor ability to activate the C–H and C–O bonds even at such a high temperature of about 650 °C. Supported monometallic Fe-based catalysts in previous studies, such as Fe/CeO_2 and Fe/Mo_2C, exhibit very low ethane conversion of only 0.5%[18] and 8%[30] at 600 °C, respectively. Carbon balance for all the experiments reached above 95% except for the monometallic Cr catalysts at 650 °C, which reached only 89% (Fig. 2), and no C3, C4, or aromatics were detected. Since the formation of coke is related to the reaction

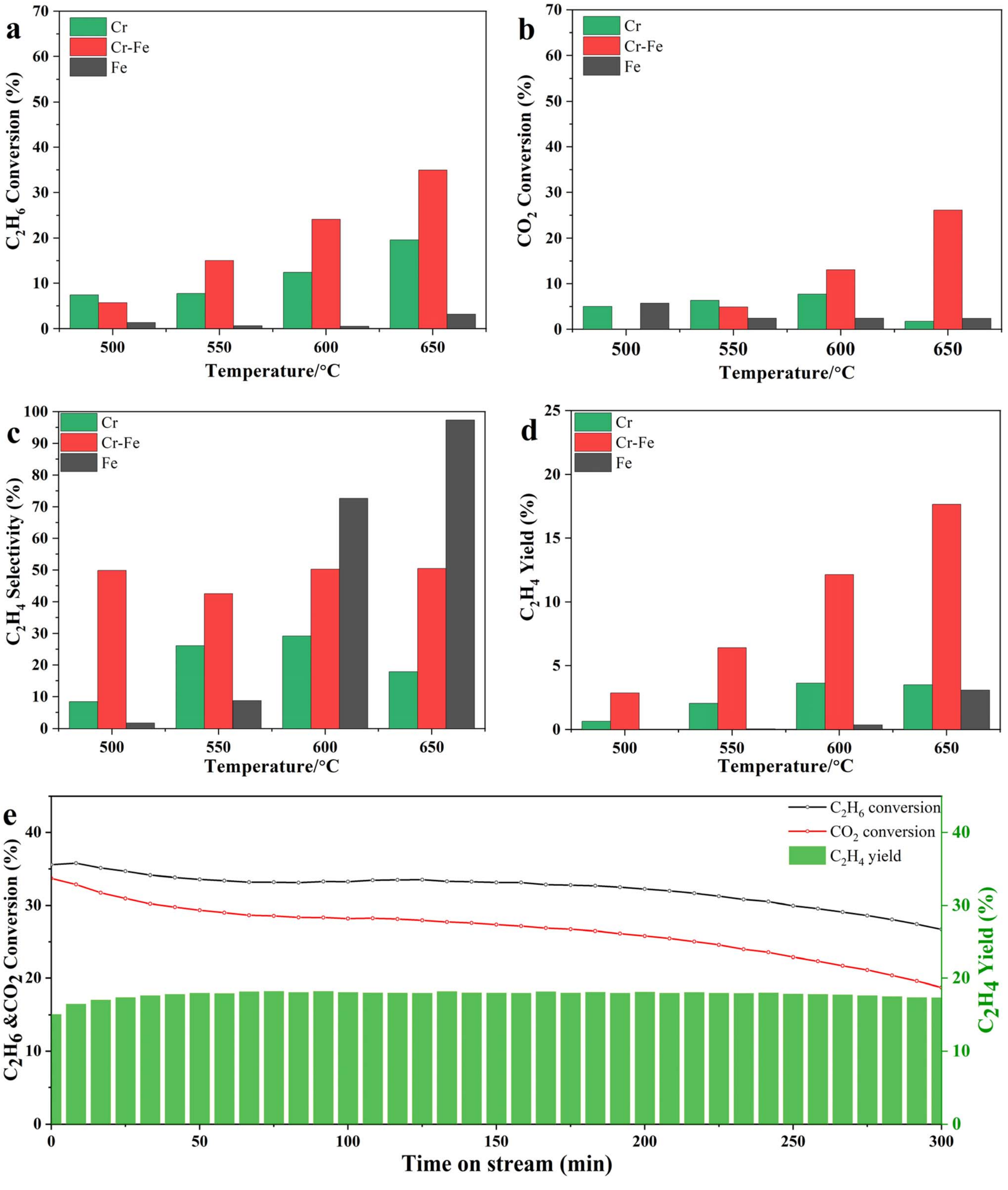

Fig. 1 Catalytic performance of the CO_2-ODHE reaction of Cr, Cr–Fe, and Fe. (a) C_2H_6 conversion, (b) CO_2 conversion, (c) C_2H_4 selectivity, (d) C_2H_4 yield, and (e) stability at 650 °C of Cr–Fe samples (space velocity: 24 000 mL g_{cat}^{-1} h^{-1}).

time, we calculated the selectivity of C_2H_4, CO, and CH_4 in the gas-phase products as the temperature increased for different catalyst samples based on the carbon balance data, as shown in Fig. 2. At the initial temperature of 500 °C, the ethylene selectivity of the Cr–Fe bimetallic oxide sample was about 56.7%, with low conversion of C_2H_6 and CO_2. As the conversion increased with temperature, the ethylene selectivity in gas-phase products decreased to 40% at 650 °C due to the

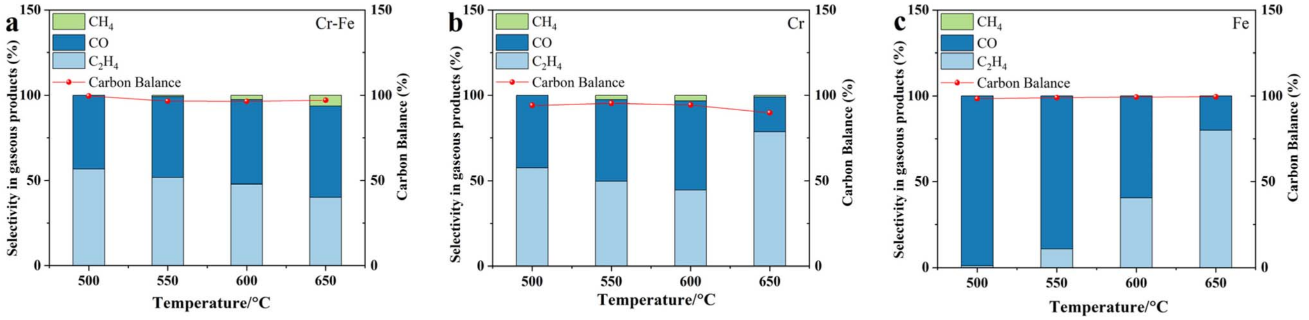

Fig. 2 Selectivity in gaseous products and carbon balance of (a) Cr–Fe, (b) Cr, and (c) Fe.

occurrence of side reactions. Although the ethylene selectivity of the monometallic Cr sample improved at 650 °C, the decline in carbon balance data indicated significant coke formation (Fig. 2b). However, taking the conversion and selectivity into consideration, the highest C_2H_4 yield can be acquired for Cr–Fe samples, reaching nearly 18% at 650 °C (Fig. 1d), which is almost the same as at 700 °C (Fig. S2). This indicates that the Cr–Fe sample exhibits excellent catalytic activity at 600–650 °C, comparable to the ethane conversion and ethylene yields of various Cr-based and Fe-based catalysts reported in the literature (Table S2). In order to exclude the influence of space velocity and inert gas dilution on the inherent activity, the reaction rates normalized by the catalyst weight were calculated. As shown in Table S1, the formation rate of ethylene of the Cr–Fe catalyst was about 13.4 $\mu mol\ g_{cat}^{-1}\ s^{-1}$, which was about 6–7 times higher than that of other reported Fe- and Cr-based catalysts. Considering the low active metal content in supported catalysts, even when normalized to a single active metal, the ethylene formation rate of the Cr–Fe sample remains comparable to others. Furthermore, on the basis of stability tests at 650 °C, a slight decrease in the conversion of C_2H_6 and CO_2 was observed. However, the C_2H_4 yield remained at 18% for 300 min.

3.2. Morphological and structural analysis before and after reaction

On the basis of the dramatic difference in catalytic performance between Fe, Cr–Fe, and Cr samples, it is significant to figure out the active site and make clear the "structure–activity" relationship in the CO_2-ODHE reaction. The powder XRD patterns of the fresh samples are shown in Fig. 3a. The monometallic Fe sample exhibits the hexagonal structure of hematite-type Fe_2O_3 (JCPDS no. 99-0060), according to the diffraction peaks at 24.2°, 33.2°, and 35.6°. Meanwhile, the peaks at 24.5°, 33.6°, and 36.2° also demonstrated a typical hexagonal structure of eskolaite-type Cr_2O_3 (JCPDS no. 38-1479) for the monometallic Cr sample. The XRD pattern of the Cr–Fe sample was different from the patterns of Fe_2O_3 and Cr_2O_3, which can be attributed to mixed oxide $(Fe,Cr)_2O_3$ (JCPDS no. 35-1112). Taking into consideration that the atomic ratio for Cr to Fe was 3 : 1, the main diffraction peaks (104) and (110) of the fresh Cr–Fe sample were closer to the peak positions of Cr_2O_3, as shown in Fig. 3b. It indicated that Fe^{3+} ions were successfully doped into the Cr_2O_3 lattice to form $(Fe,Cr)_2O_3$ oxide solid solution in the fresh Cr–Fe sample because of the similar ionic radii of the Fe^{3+} (0.645 Å) and Cr^{3+} (0.615 Å) cations.[31] XRD peak broadening is mainly related to the inhomogeneity of the cell size resulting from spatial variations in the amount and distribution of cations and vacancies in Cr^{3+} and Fe^{3+}.[32] Consequently, all three samples exhibited the same hexagonal lattice structure. Furthermore, the average particle sizes of all fresh samples were calculated using the Scherrer formula, yielding about 48 nm, 28 nm, and 24 nm for Fe, Cr–Fe, and Cr samples, respectively. It showed that the monometallic Cr sample possesses better anti-sintering ability compared to the monometallic Fe sample, which can also explain the smaller particle size of the fresh Cr–Fe sample due to the formation of a $(Fe,Cr)_2O_3$ solid solution. Thus, the formation of the $(Fe,Cr)_2O_3$ solid solution oxide leads to lattice distortion and an increase in lattice defects, inhibiting grain growth and reducing the grain size of Cr–Fe samples. The smaller grain size indicates more exposed active sites, which is beneficial for catalytic reactions.

Taking the high reaction temperature and complex gas atmosphere of the CO_2-ODHE reaction into consideration, dramatic structural evolution may occur during the reaction. From the XRD patterns of all used samples (Fig. 3c), it is evident that the CO_2-ODHE reaction induces significant phase transformations in the Fe-containing catalyst samples. For the Fe-used sample, the peaks at 18.4°, 30.2°, and 35.3° can be attributed to the (111), (220), and (311) planes of cubic phase Fe_3O_4 (JCPDS no. 99-0073). It indicated that Fe_2O_3 was reduced to Fe_3O_4 during H_2 pre-activation and the reaction process. Using the Scherrer formula, the grain size of the monometallic Fe sample was ∼60 nm after the reaction, suggesting the obvious agglomeration along with the phase transformation during the reaction. For the monometallic Cr sample (initial phase: Cr_2O_3), the XRD pattern demonstrated the stability of the Cr_2O_3 phase after the H_2 pre-activation and the reaction process. However, the particle size of Cr_2O_3 increased notably from 24 nm to 36 nm after the reaction. For the Cr–Fe-used sample, there were new diffraction peaks at 18.3°, 30.1°, 35.5°,43.1°, 57.1° and 62.6°, indicating the formation of the spinel-structured $FeCr_2O_4$ component (JCPDS no. 99-0030) with an average particle size of 20.8 nm.[33] Compared with used monometallic Fe and Cr samples, the $FeCr_2O_4$ component

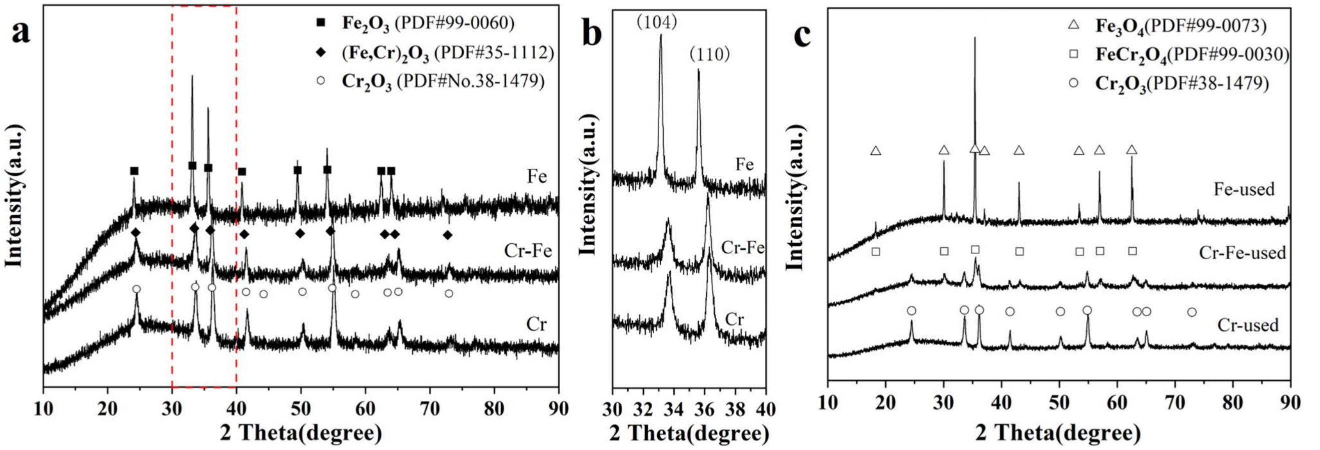

Fig. 3 (a)XRD patterns of fresh $FeCrO_x$ catalysts, (b) the magnified portion of the curve in the 30–40° range in (a), and (c) XRD patterns of used $FeCrO_x$ catalysts.

exhibited a better anti-sintering ability. In addition, there was also isolated Cr_2O_3 phase in the Cr–Fe-used sample due to the high ratio of Cr/Fe of about 3 : 1. Thus, it can be preliminarily determined that the formation of $FeCr_2O_4$ could improve the catalytic activity of the Cr–Fe sample in the CO_2-ODHE reaction. Additionally, the material synthesized with the initial Cr/Fe molar ratio of 2 : 1 was also evaluated to identify the main active phase during the reaction. It was observed that at 650 °C, the ethane conversion (34%), CO_2 conversion (26%), and ethylene yield (17%) over the 2 : 1 catalyst were largely consistent with those of the 3 : 1 catalyst (Fig. S1). Furthermore, even in the Cr_2Fe_1-used sample, a small amount of Cr_2O_3 was detected by XRD (Fig. S3), indicating incomplete consistency with the initial stoichiometric ratio. Nevertheless, the similar catalytic performance in both samples strongly supports that the active species is the spinel-structured $FeCr_2O_4$, despite the notably lower content of Cr_2O_3 in the Cr_2Fe_1-used sample compared to the Cr_3Fe_1-used sample.

In consideration of incomplete dissolution in ICP-OES tests and structural homogeneity for the Cr–Fe sample, the quantitative analysis of iron and chromium elements was performed using XPS fitting results. As shown in Table 1, the surface atomic ratio of Fe to Cr in the Cr–Fe catalyst is 23.1 : 76.9, well consistent with the designed value, verifying the effectiveness of the two-step urea hydrolysis method. Furthermore, the pore structure and specific surface area of the fresh samples were characterized using N_2 physical adsorption experiments. The specific surface areas of the fresh Fe, Cr–Fe, and Cr samples are 13 $m^2\ g^{-1}$, 51 $m^2\ g^{-1}$, and 39 $m^2\ g^{-1}$, respectively. The nitrogen adsorption and desorption isotherms of all catalysts exhibit type V curves, indicating weak interactions between the adsorbent and the adsorbate. The presence of hysteresis loops is caused by the inter-particle pores (Fig. S4). The BJH average pore diameter of the fresh Cr–Fe sample was 20.9 nm, which is significantly smaller than those of the monometallic Fe (44.75 nm) and monometallic Cr (32.13 nm) samples. The particle size of all fresh samples was well consistent with the XRD results. Therefore, the Cr–Fe sample exhibits a higher specific surface area and a smaller particle size than those of the monometallic Fe and Cr samples, which may be beneficial for the adsorption and activation of reactant molecules.

Fig. 4 shows the SEM images of the Fe, Cr–Fe, and Cr catalysts before and after the reaction. It can be seen that the morphology of the three fresh samples was quite similar, all approximately spherical and uniform in size, with secondary particle sizes ranging from several tens to a hundred nanometers, as shown in Fig. 4a(1)–c(1). However, after the CO_2-ODHE reaction at 700 °C, there is significant agglomeration and growth in the particle size of the monometallic Fe sample (Fig. 4a(2)), with morphology changing from spherical to

Table 1 Surface atomic ratio, BET surface area, BJH pore size distribution (r_p), crystallite size of fresh $FeCrO_x$ catalysts and phase composition and crystallite size of used $FeCrO_x$ Catalysts

Sample	Surface atomic ratio (Fe/Cr)[a]	S_{BET}[b] ($m^2\ g^{-1}$)	r_p[b] (nm)	D_{fresh}[c] (nm)	Phase composition after the reaction	D_{used}[d] (nm)
Fe	100/0	13	44.75	48	Fe_3O_4	60
Cr–Fe	23.1/76.9	51	20.9	28	$FeCr_2O_4/Cr_2O_3$	20.8/28.9
Cr	0/100	39	32.13	24	Cr_2O_3	36.8

[a] Determined by XPS. [b] Calculated from nitrogen adsorption–desorption results. [c] Calculated from the Scherrer formula at the (104) crystal plane of $(Fe,Cr)_2O_3$. [d] Calculated from the Scherrer formula at the related phase in used catalysts.

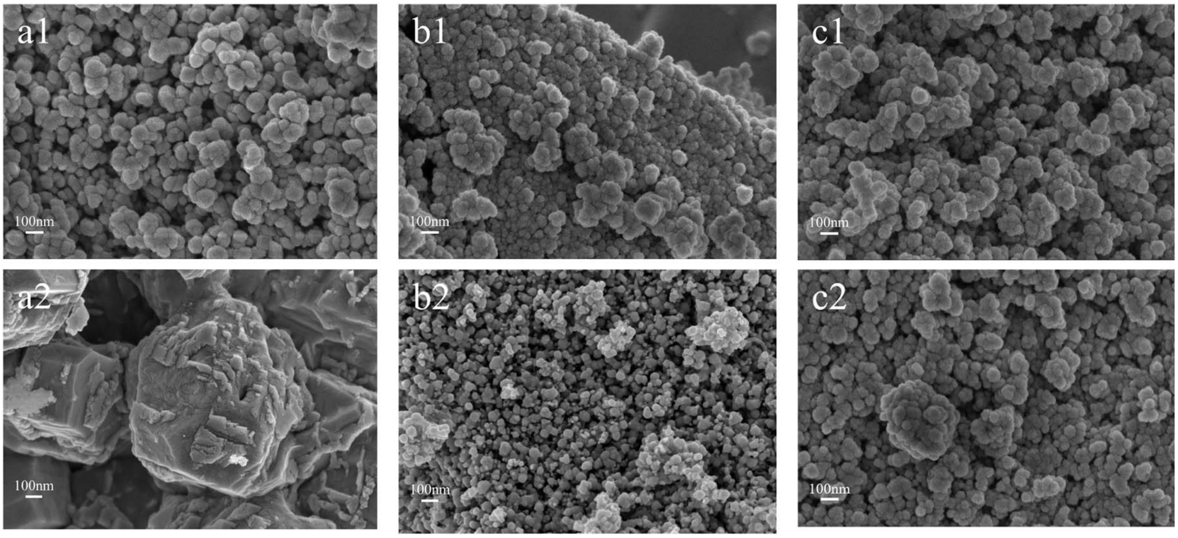

Fig. 4 SEM images of $FeCrO_x$ catalyst samples (1) before and (2) after the reaction: (a) Fe, (b) Cr–Fe, and (c) Cr.

angular polygons because of the low melting point of iron oxide and high diffusion rate of iron ions during the transformation of Fe_2O_3 into Fe_3O_4.[34,35] In contrast, the spherical morphology of Cr and Cr–Fe samples can be well maintained without obvious aggregation after the CO_2-ODHE reaction. It further shows the good anti-sintering ability for the formation of $FeCr_2O_4$.

Meanwhile, the TEM and HRTEM characterization studies further provided the detailed information about the morphology, size, and shape of the Cr–Fe-used sample under a microdomain view (Fig. 5). The TEM image in Fig. 5a shows that the Cr–Fe-used sample is composed of polyhedron-like nanoparticles with an average particle size of ~25.5 ± 8.0 nm, in good agreement with XRD results. In the high-resolution TEM images, two distinct lattice fringes were clearly visible, in which the interplanar distances of 0.36 nm and 0.48 nm were attributed to the (012) plane of Cr_2O_3 and the (111) plane of $FeCr_2O_4$, respectively. Taking the particle size of the active site over 20 nm, an area of about 70 nm^2 was chosen to conduct the EDS mapping experiment (Fig. 5c) to ensure data reliability. It indicated that the Cr and Fe elements were distributed uniformly in the component of $FeCr_2O_4$ in some areas, with isolated Cr element in other areas from Cr_2O_3. It further demonstrated that $FeCr_2O_4$ was stable after the CO_2-ODHE reaction.

Fig. 6 presents the Raman spectra for the Fe, Cr, and Cr–Fe samples before and after the reaction to provide fine surface structural information. The Raman spectrum of the fresh Fe sample displayed typical features of Fe_2O_3, with notable peaks at 224, 245, 292, 407, 496, and 609 cm^{-1}, corresponding to the six vibrational modes ($A_{1g}(1)$, $E_g(1)$, $E_g(2)$, $E_g(3)$, $E_g(4)$, and $A_{1g}(2)$)[21,36] shown in Fig. 6a. The fresh Cr sample exhibited characteristic Raman peaks of Cr_2O_3, occurring at 304 cm^{-1} (E_g), 341 cm^{-1} (E_g), 537 cm^{-1} (A_g), and 592 cm^{-1} (E_g)[36–38] (Fig. 6b). For the Cr–Fe mixed sample, the most evident difference in the spectrum of the Cr–Fe mixed oxide compared to its parent binary oxides is the presence of a very strong band in the region of 560–700 cm^{-1}, which is completely absent in the monometallic oxides and is indicative of the characteristic peak of $FeCrO_x$ mixed oxide[37,39] (Fig. 6c). Previous studies have indicated that this strong band is associated with magnons, which represent collective excitations of electron spins and anisotropic magnetic interactions within the lattice framework.[36,38,40]

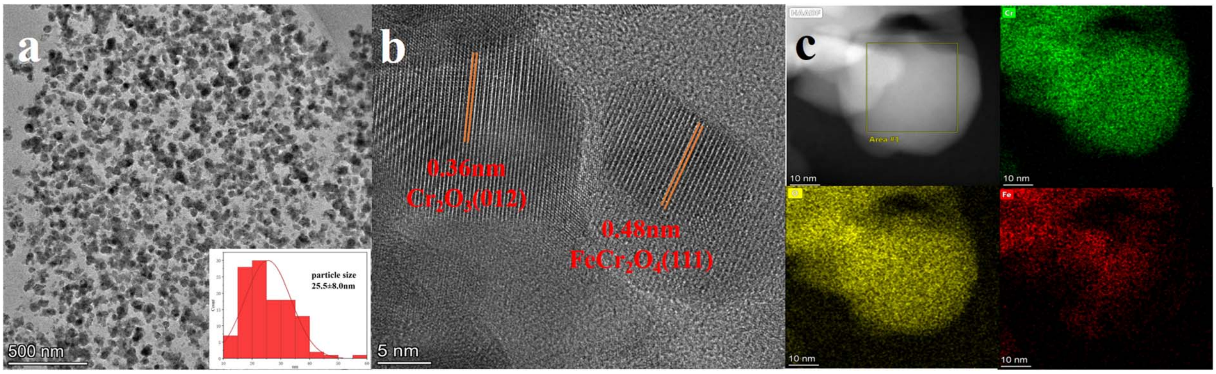

Fig. 5 (a) TEM, (b) high-resolution TEM images and (c) elemental mapping images of the Cr–Fe-used catalyst.

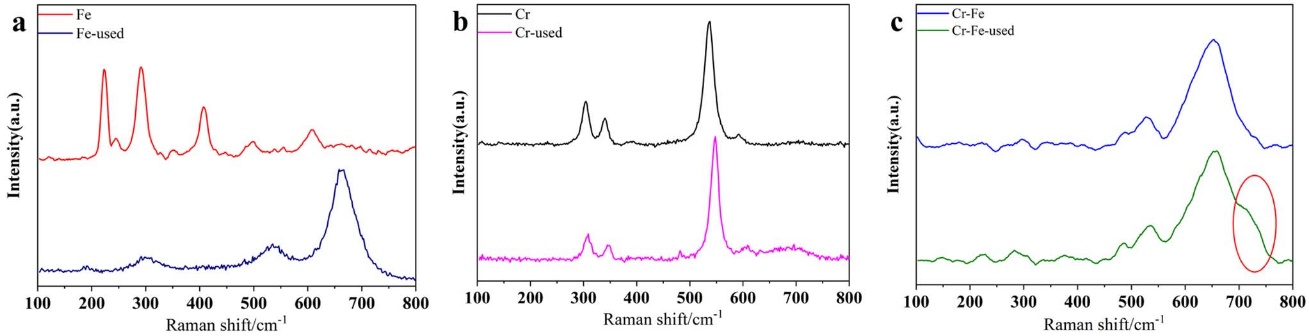

Fig. 6 Raman patterns of (a) Fe, (b) Cr, and (c) Cr–Fe catalysts before and after the reaction.

After the reaction, the Raman spectrum of the Fe-used sample shows significant changes with peaks at 299, 534, and 662 cm^{-1}, corresponding to Fe_3O_4.[37,39] In contrast, the Cr-used sample shows a blue shift in the characteristic vibrational peaks of Cr_2O_3, indicating the decrease of oxygen vacancies on the catalyst surface after the reaction.[41] Notably, the peak positions of the Cr–Fe-used sample do not show a significant shift after the CO_2-ODHE reaction, however, a prominent shoulder appears at 695–750 cm^{-1}, confirming the presence of the spinel phase $FeCr_2O_4$ (ref. 21, 37, 39 and 42) in the Cr–Fe-used sample.

The element-sensitive XAFS technique was used to determine the precise electronic and local coordination structures of the Fe and Cr species in used Fe, Cr–Fe, and Cr catalysts. The near-edge region (XANES) of the XAFS spectra provided electronic information about the metal atoms under investigation. The absorption edge energy, white line peak intensity, and pre-

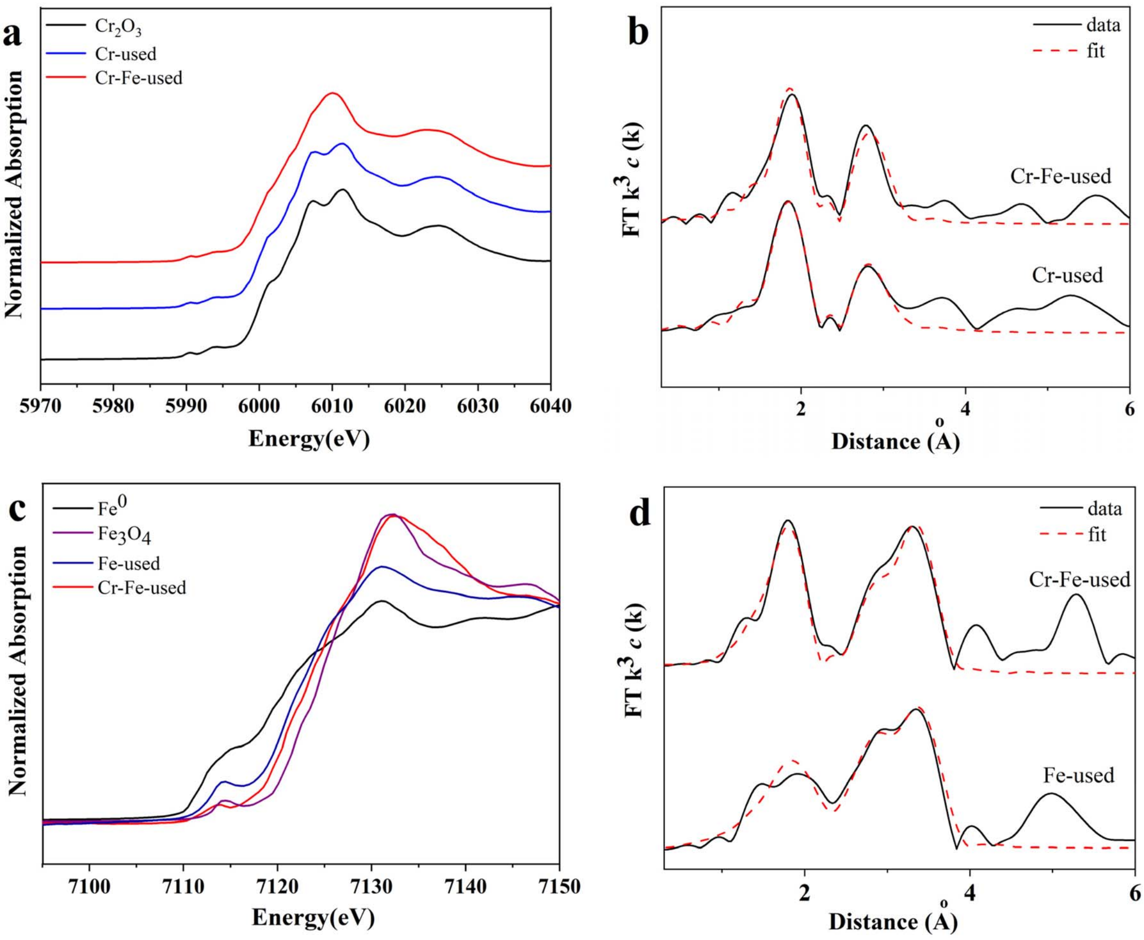

Fig. 7 Cr K-edge: (a) XANES profiles and (b) EXAFS fitting results; Fe K-edge: (c) XANES profiles and (d) EXAFS fitting results in *R* space of used $FeCrO_x$ catalysts.

edge features are all related to the oxidation state of the metal. The XANES spectra of Cr-used and Cr–Fe-used samples shown in Fig. 7a indicate that the average oxidation state of the Cr element in Cr-containing samples was +3, without further being reduced into the metallic Cr state during the reaction. According to XRD and HRTEM results, the Cr species was involved in the formation of Cr_2O_3 and $FeCr_2O_4$ in the Cr–Fe-used sample. There was a strong Cr–O shell at ~2.0 Å with a coordination number of 6.4 ± 0.7 and 6.7 ± 0.6 for Cr-used and Cr–Fe-used samples, respectively. For the second shell, a coordination structure of Cr–O–Cr at ~2.95 Å can be fitted for Cr-used and Cr–Fe-used samples, in which the coordination number of the Cr–O–Cr/Fe shell for Cr-used (~2.5) and Cr–Fe-used (~4.5) samples was obviously different (Fig. 7b and Table S3). It further demonstrated that $FeCr_2O_4$ possessed a different coordination structure with Cr_2O_3.

Furthermore, the Fe K-edge (7112 eV) XAFS measurements of the Fe-used and Cr–Fe-used catalysts were also conducted as shown in Fig. 7c and d and Table S4. The edge jump energies of the Fe-used and Cr–Fe-used catalysts were between those of Fe-foil and Fe_3O_4. The average oxidation state of iron for the Fe-used and Cr–Fe-used catalysts was +2.2 and +2.6, respectively, calculated from linear combination fitting results shown in Fig. S5 and Table S4. The EXAFS spectra of the Fe-used and Cr–Fe-used samples shown in Fig. 7d exhibited the coordination structure of Fe species. For the Fe-used sample, the Fe–O ($R \approx$ 2.0 Å, CN ≈ 3.9), Fe–O–Fe1 ($R \approx$ 2.97 Å, CN ≈ 3.9) and Fe–O–Fe2 ($R \approx$ 3.49 Å, CN ≈ 11.6) shells were acquired, which were assigned to the typical Fe_3O_4 structure. In addition, a tiny metallic Fe–Fe ($R \approx$ 2.52 Å, CN ≈ 1.2) shell was necessary for the fitting data of Fe-used sample, which was well consistent with the lower average oxidation state over iron species. For the Cr–Fe-used sample, the coordination number of the Fe–O shell at $R \approx$ 1.94 Å increased to 5.4. Moreover, there were Fe–O–Fe1 ($R \approx$ 2.92 Å, CN ≈ 2.4) and Fe–O–Cr ($R \approx$ 3.47 Å, CN ≈ 12.1) shells for the fitting results. According to XAFS results, it can be seen that there were more oxygen atoms surrounding Fe species in $FeCr_2O_4$, which may be beneficial for the elimination of deposited coke. Based on the combined results of XRD, HRTEM and XAFS results, we can confirm that the main active sites in Fe, Cr–Fe and Cr samples are Fe_3O_4, $FeCr_2O_4$ and Cr_2O_3, respectively.

Additionally, the phase transformation process of the Cr–Fe catalyst from hydrogenation pretreatment to the CO_2-ODHE reaction was *in situ* monitored by synchrotron radiation XRD (SR-XRD). The 2D-XRD pattern exhibits distinct concentric rings, with a non-uniform intensity distribution of the diffraction rings observed within the azimuthal angle range of 0°–180°, indicating a preferred orientation of the crystals along specific crystal planes (Fig. 8). Through radial integration, the 2D image was converted into a 1D diffraction pattern. As expected, the fresh sample exhibited clearly visible diffraction rings, ordered from the center outward, corresponding to the diffraction peaks at 24.3, 33.5, 35.9, 41.2, 49.8, and 54.6°, which are indexed to the (012), (104), (110), (113), (024), and (116) crystal planes of the $(Fe,Cr)_2O_3$ (JCPDS no. 35-1112) solid solution at room temperature (Fig. 8a and b), respectively. After the reduction, the $(Fe,Cr)_2O_3$ solid solution was gradually reduced to Fe^0 (JCPDS no. 06-0696) with the appearance of an additional diffraction ring at 44.5° (indicated by an arrow in Fig. 8c). The diffraction peaks at 24.5, 33.6, and 36.2° of Cr_2O_3 (JCPDS no. 38-1479) became distinctly visible. Upon switching to the reaction atmosphere, the disappearance of the Fe^0 diffraction peak at 44.5° indicates that Fe^0 cannot remain stable under the reaction conditions in the presence of the oxidizing CO_2 atmosphere. The absence of diffraction peaks at 33.4, 41.2, and 49.8° signified the complete disappearance of the $(Fe,Cr)_2O_3$ solid solution phase, and the new diffraction peaks at 30.1, 35.5, and 57.1° just appeared, corresponding to the diffraction ring observed at the position indicated by the arrow in Fig. 8d, indicating the formation of $FeCr_2O_4$ under the reaction conditions. Furthermore, with the progress of reaction, the $FeCr_2O_4$ component was generated and maintained for the whole reaction.

Moreover, when the pretreatment gas was altered to air and inert gas (Ar) instead of the reducing hydrogen atmosphere (Fig. S6), it was observed that a reducing pretreatment atmosphere slightly favored the conversion of ethane compared to the others at lower temperatures, suggesting that the reductive pretreatment atmosphere promotes the phase transformation process, thereby effectively shortening the induction period for the generation of the active phase. Notably, even when oxidative (air) or inert (Ar) atmospheres are used instead of H_2 pretreatment, the $FeCr_2O_4$ phase remains stable after the reaction (Fig. S7), which may be due to the inevitable generation of reductive H_2 in the CO_2-ODHE reaction. Therefore, the *in situ* XRD experiments further confirmed the generation of spinel-structured $FeCr_2O_4$ during the CO_2-ODHE reaction, which had previously been identified as the active phase for this reaction through TEM and Raman characterization.

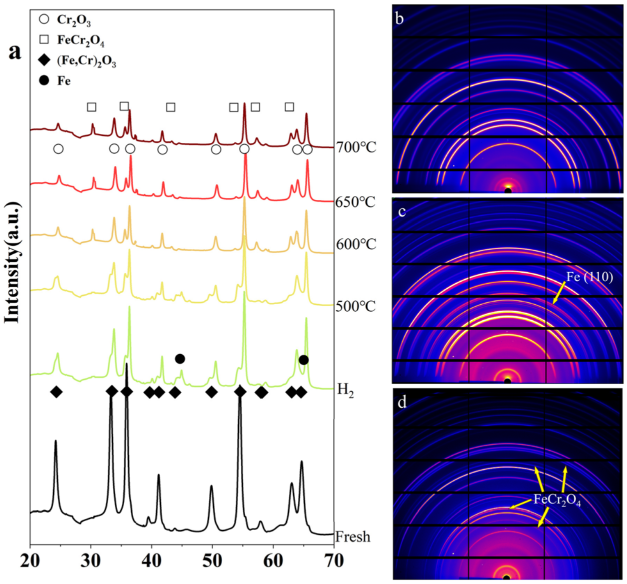

Fig. 8 *In situ* SR-XRD (a) patterns of the Cr–Fe catalyst during the CO_2-ODHE reaction and 2D images of (b) fresh catalyst (c) after pretreatment at 450 °C in 50% H_2/Ar and (d) at 650 °C in the reaction gases ($CO_2/C_2H_6/Ar$ = 10/10/20 mL min^{-1}).

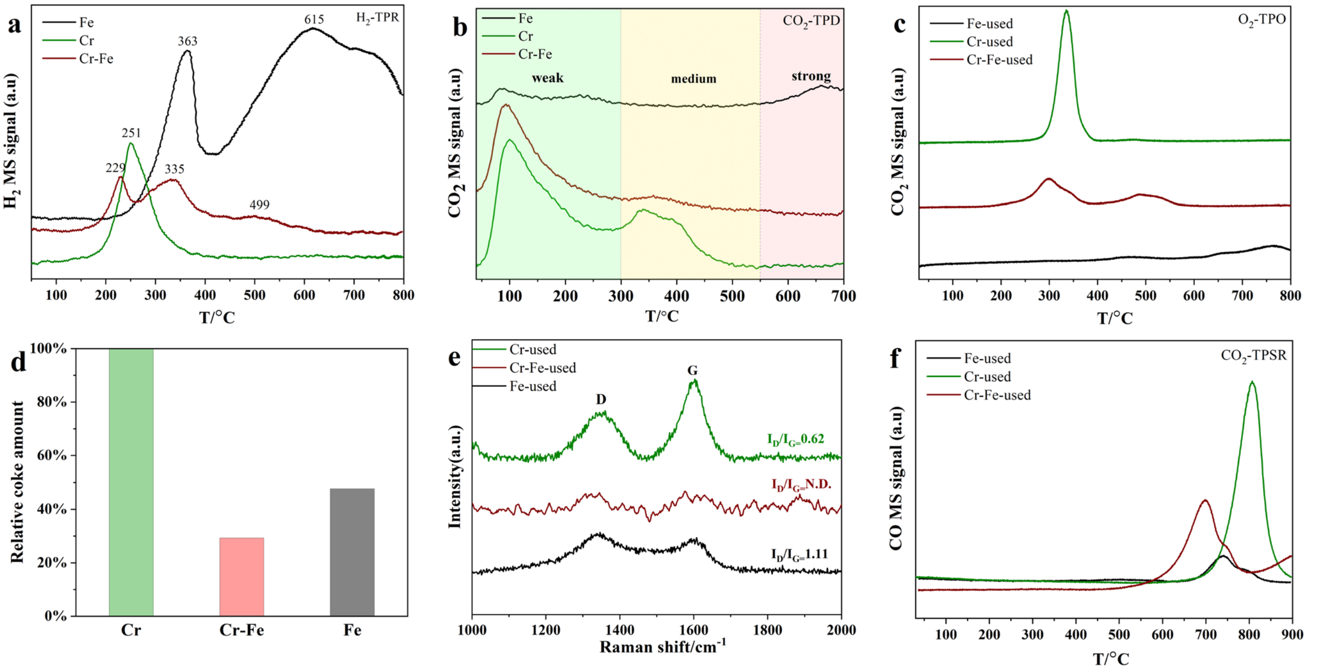

Fig. 9 (a) H_2-TPR of fresh $FeCrO_x$ samples, (b) CO_2-TPD of $FeCrO_x$ samples, (c) O_2-TPO and (f) CO_2-TPSR of the used $FeCrO_x$ samples, (d) the estimated relative coke deposition on the catalyst from (c), and (e) Raman spectra of used $FeCrO_x$ samples in the wavenumber range of 1000–2000 cm^{-1}.

3.3. Catalyst reaction mechanism

To further investigate the reducibility and metal-oxide interaction of the $FeCrO_x$ catalysts, H_2-TPR characterization was conducted on the Fe, Cr, and Cr–Fe samples. As shown in Fig. 9a, the fresh Fe sample exhibits two peaks at 363 °C and after 400 °C (with a peak centered at 615 °C). The first peak was assigned to the reduction of Fe_2O_3 to Fe_3O_4, while the latter peak (after 400 °C) can be attributed to the reduction of Fe_3O_4 to Fe^{2+} and Fe^0.[43–45] For the fresh Cr sample, only a reduction peak at 251 °C can be observed, originating from the reduction of surface Cr^{6+} species to Cr^{3+}, which are reported to coexist on the catalyst surface under oxidizing conditions[12,14] and are reduced at relatively low temperatures (200–300 °C).[21,35,46] For the fresh Cr–Fe samples, the reduction peaks at 229, 335 and 499 °C were attributed to the reduction of surface Cr^{6+} species, Fe^{3+} to Fe^{2+} and Fe^0, which were much lower than those in monometallic Fe and Cr samples. It indicated that the formation of the $(Fe,Cr)_2O_3$ solid solution can improve the reducibility of Fe and Cr species.

We used CO_2-TPD experiments to characterize the CO_2 adsorption capacity of active site properties for different catalysts. The basicity of catalysts, which can be correlated with their CO_2 desorption temperature, is typically categorized as follows: weak (<300 °C), medium (300–500 °C) and strong (>500 °C). Prior to TPD, the catalyst sample was processed with 5% H_2/Ar (50 mL min^{-1}) at 450 °C for 90 min. As shown in Fig. 9b and Table 2, the Fe sample exhibits tiny CO_2 desorption peaks at 90 °C and 660 °C, indicating the weak CO_2 adsorption capacity of Fe_3O_4. It was also in agreement with the catalytic performance, in which the Fe catalyst exhibited low CO_2 conversion. For the Cr catalyst, the CO_2 desorption peaks occurred primarily at 100 °C and 338 °C, which are assigned to weak and medium basic sites, respectively. This demonstrates that Cr_2O_3 is beneficial for adsorbing CO_2 to participate in the CO_2-ODHE reaction, thereby contributing to the higher CO_2 conversion over the Cr catalyst (Fig. 1b). However, for the Cr–Fe sample, only a visual and strong CO_2 adsorption peak at ~100 °C can be detected, suggesting weak basicity on $FeCr_2O_4$, in which the weak basicity may be a key factor in the higher C_2H_4 yield for the Cr–Fe sample. The presence of weak basic sites improved selectivity to alkene and reduced coke formation.[47] In contrast, the strong basic sites favor the side reactions, such as reforming and cracking reactions, leading to significant coke deposition and reduced reaction activity.[14] The He-TPSR experiments confirmed that both the Cr_2O_3 and $FeCr_2O_4$ catalysts contain certain active oxygen species capable of reacting with deposited coke, exhibiting similar light-off temperatures (Fig. S8). However, CO_2 molecules adsorbed on the weak and medium basic sites should be relatively active and can readily participate in reactions, especially the weak basic sites.[48] Therefore, the Cr–Fe sample exhibits superior CO_2 adsorption

Table 2 CO_2 desorption peak area for $FeCrO_x$ catalysts[a]

Sample	$S_{weak}/S_{medium}/S_{strong}$ ($\times 10^{-7}$)
Fe	2.6/0/0.6
Cr–Fe	12.5/0.3/0
Cr	18.5/3.2/0

[a] Estimated by CO_2-TPD.

and activation capabilities, attributable to its weak basic sites. This property facilitates the gasification of carbon deposits, thereby effectively mitigating coke accumulation. Furthermore, the O_2-TPO experiment also certified the lowest amount of coke deposition in the Cr–Fe-used sample (Fig. 9c). Generally, the carbon species with a lower peak temperature shows a higher activity and can be easily removed.[18,49] For the Cr-used sample, a strong CO_2 peak at 330 °C can be observed, which was well consistent with the low carbon balance shown in Fig. 2b. Furthermore, two peaks at ~300 °C and 500 °C were acquired in the Cr–Fe-used sample, which can be attributed to the oxidation of coke on Cr_2O_3 and $FeCr_2O_4$ respectively, with much less coke deposition on $FeCr_2O_4$. For Fe-used samples, the amount of coke deposited is small because of low activity in the CO_2-ODHE reaction. By integrating the CO_2 peaks from the mass spectrometry data and normalizing against the ethane conversion rate, we compared the relative coke amounts per unit mass of used catalysts (Fig. 9d). The monometallic Cr-used sample exhibited the highest quantity of coke deposition, despite its lower activity compared to the Cr–Fe-used catalysts, due to its medium basicity. The Raman spectra of used samples (Fig. 9e) also showed that the Fe-used and Cr-used samples exhibited prominent D bands (disorder-induced, ~1430 cm^{-1}) and G bands (in-plane vibrations, ~1610 cm^{-1}) associated with coke deposition.[50] However, these tiny peaks at ~1430 cm^{-1} and ~1610 cm^{-1} in the Cr–Fe-used sample made it impossible to evaluate the degree of carbon graphitization using the I_D/I_G intensity ratio value. In addition, the conversion of CO_2 plays a key role in the elimination of coke deposition in the CO_2-ODHE reaction through the oxidation of coke by the CO_2 molecule. In Fig. 9f, it can be seen that CO_2 can react with surface deposited coke to release CO at 550 °C in the Cr–Fe-used sample, continuing up to 800 °C. The results indicate that $FeCr_2O_4$ can effectively activate CO_2 molecules, enabling the Boudouard reaction ($C + CO_2 \rightarrow 2CO$) with deposited coke even at relatively low temperatures. Moreover, CO_2 in the reaction stream continuously reacts with carbon deposits across the entire temperature range of the CO_2-ODHE reaction (500–700 °C), thereby contributing to the improvement of catalytic performance. In contrast, significant CO release for the monometallic catalyst samples was observed only at 700 °C. Despite the continuous oxygen supply from CO_2 before this temperature, it could not react with the surface coke on the catalysts, aligning with the observed reaction activity. Based on these results, it can be concluded that the $FeCr_2O_4$ phase effectively adsorbs and activates CO_2, thereby facilitating coke removal and promoting the CO_2-ODHE reaction.

Additionally, the Cr–Fe sample that lost activity after the stability test (650 °C, >12 h) was regenerated by calcining in air at 600 °C to remove coke (Fig. S9a). Subsequent stability tests showed that the initial conversion rates and yields were restored but revealed recurring deactivation patterns with continued reaction, indicating that the gradual accumulation of coke is the primary cause of $FeCrO_x$ catalyst deactivation. Significantly, CO_2-TPSR results demonstrate the ability of $FeCr_2O_4$ to activate CO_2 for low-temperature carbon gasification. To validate this *in situ* regeneration strategy, we performed cyclic CO_2 treatments on deactivated catalysts (Fig. S9b). Each regeneration cycle substantially restored ethane conversion (>95% recovery) while maintaining ethylene yield above 15% throughout repeated testing. These findings collectively establish continuous CO_2 purging as a promising operational strategy to mitigate coke-induced deactivation during the reaction.

4. Conclusions

In summary, nano-iron oxide, chromium oxide, and FeCr bimetallic oxides were synthesized using a two-step urea precipitation method and subjected to CO_2 oxidative dehydrogenation of ethane catalytic tests. The Cr–Fe sample exhibited significantly higher activity compared to the monometallic samples with the conversion of ethane and CO_2 approaching 35% and 27% at 650 °C, respectively. And the formation rate of C_2H_4 was about 13.4 μmol g_{cat}^{-1} s^{-1} with the C_2H_4 yield remaining at 18% for 300 min. Through XRD, Raman, SEM and XAFS characterization, it was found that the monometallic Fe sample transformed from Fe_2O_3 to Fe_3O_4 during the reaction and underwent sintering. Although the monometallic Cr sample did not show significant phase changes, it tends to deactivate due to substantial coke formation. In contrast, the bimetallic Cr–Fe sample formed a solid solution oxide of $(Fe,Cr)_2O_3$, effectively reducing the catalyst grain size and resisting sintering. The *in situ* formation and stable spinel structure of $FeCr_2O_4$ during the reaction, which were characterized by synchrotron radiation-based *in situ* XRD, confirm that $FeCr_2O_4$ is the active phase for the CO_2-ODHE reaction. Moreover, the Cr–Fe sample with weak basic sites exhibits superior CO_2 adsorption and activation capabilities. According to O_2-TPO and CO_2-TPSR of the used samples, $FeCr_2O_4$ enables the combustion of coke deposited on the catalyst surface at lower temperatures, thus significantly enhancing the reaction activity and regeneration stability. Our work may provide theoretical guidance for the industrial application of non-noble metal catalysts in CO_2 oxidative dehydrogenation of ethane.

Conflicts of interest

There are no conflicts to declare.

Data availability

The authors confirm that the data supporting the findings of this study are available within the article and its SI. See DOI: **https://doi.org/10.1039/d5ta05111h**.

Acknowledgements

This work was supported by the "Photon Science Research Center for Carbon Dioxide", "Project of the National Natural Science Foundation of China" (22332003 and 12505386), Science and Technology Innovation Plan of Shanghai Science and Technology Commission (23YF1453700), "Shanghai Municipal Science and Technology Commission" (23JC1403300), "2025 Research Equipment Project of the

Special Fund for Improving Research Conditions in Central-Level Scientific Institutions, Chinese Academy of Sciences" and "Shanghai Municipal Science and Technology Major Project". We appreciate the assistance of TILON Group Technology Limited (Division of China) in characterization of catalysts. Additionally, the User Experiment Assist System (**https://cstr.cn/31124.02.SSRF.LAB**), 14W1, 02U2, 13SSW, 17B, and 16U1 beamline of SSRF provided support for data collection for this work.

References

1 J. F. S. de Oliveira, D. P. Volanti, J. M. C. Bueno and A. P. Ferreira, Effect of CO_2 in the oxidative dehydrogenation reaction of propane over Cr/ZrO_2 catalysts, *Appl. Catal., A*, 2018, **558**, 55–66, DOI: **10.1016/j.apcata.2018.03.020**.

2 G.-Q. Yang, H. Wang, T. Gong, Y.-H. Song, H. Feng, H.-Q. Ge, H.-b. Ge, Z.-T. Liu and Z.-W. Liu, Understanding the active-site nature of vanadia-based catalysts for oxidative dehydrogenation of ethylbenzene with CO_2 *via* atomic layer deposited VO_x on γ-Al_2O_3, *J. Catal.*, 2019, **380**, 195–203, DOI: **10.1016/j.jcat.2019.10.009**.

3 L.-C. Wang, Y. Zhang, J. Xu, W. Diao, S. Karakalos, B. Liu, X. Song, W. Wu, T. He and D. Ding, Non-oxidative dehydrogenation of ethane to ethylene over ZSM-5 zeolite supported iron catalysts, *Appl. Catal., B*, 2019, **256**, 117816, DOI: **10.1016/j.apcatb.2019.117816**.

4 Y. Zhang, M. Chen, W. Wang and Y. Zhang, A stable Pt modified cobalt tungstate catalyst for CO_2-assisted oxidative dehydrogenation of ethane, *Catal. Sci. Technol.*, 2024, **14**(14), 3924–3935, DOI: **10.1039/d4cy00399c**.

5 E. Gomez, B. Yan, S. Kattel and J. G. Chen, Carbon dioxide reduction in tandem with light-alkane dehydrogenation, *Nat. Rev. Chem.*, 2019, **3**(11), 638–649, DOI: **10.1038/s41570-019-0128-9**.

6 P. Liu, L. Zhang, M. Li, N. Sun and W. Wei, Recent progress in Cr-based catalysts for oxidative dehydrogenation of light alkanes by employing CO_2 as a soft oxidant, *Clean Energy*, 2021, **5**(4), 623–633, DOI: **10.1093/ce/zkab036**.

7 T. A. Bugrova, V. V. Dutov, V. A. Svetlichnyi, V. Cortés Corberán and G. V. Mamontov, Oxidative dehydrogenation of ethane with CO_2 over CrO_x catalysts supported on Al_2O_3, ZrO_2, CeO_2 and $Ce_xZr_{1-x}O_2$, *Catal. Today*, 2019, **333**, 71–80, DOI: **10.1016/j.cattod.2018.04.047**.

8 Y. Gambo, S. Adamu, G. Tanimu, I. M. Abdullahi, R. A. Lucky, M. S. Ba-Shammakh and M. M. Hossain, CO_2-mediated oxidative dehydrogenation of light alkanes to olefins: advances and perspectives in catalyst design and process improvement, *Appl. Catal., A*, 2021, **623**, 118273, DOI: **10.1016/j.apcata.2021.118273**.

9 M. Maroño, E. Ruiz, J. M. Sánchez, C. Martos, J. Dufour and A. Ruiz, Performance of Fe–Cr based WGS catalysts prepared by co-precipitation and oxi-precipitation methods, *Int. J. Hydrogen Energy*, 2009, **34**(21), 8921–8928, DOI: **10.1016/j.ijhydene.2009.08.068**.

10 M. D. Porosoff, M. N. Z. Myint, S. Kattel, Z. Xie, E. Gomez, P. Liu and J. G. Chen, Identifying Different Types of Catalysts for CO_2 Reduction by Ethane through Dry Reforming and Oxidative Dehydrogenation, *Angew. Chem., Int. Ed.*, 2015, **54**(51), 15501–15505, DOI: **10.1002/anie.201508128**.

11 Y. Cheng, H. Gong, C. Miao, W. Hua, Y. Yue and Z. Gao, Ga_2O_3/HSSZ-13 for dehydrogenation of ethane: effect of pore geometry of support, *Catal. Commun.*, 2015, **71**, 42–45, DOI: **10.1016/j.catcom.2015.08.015**.

12 S. Wang, K. Murata, T. Hayakawa, S. Hamakawa and K. Suzuki, Dehydrogenation of ethane with carbon dioxide oversupported chromium oxide catalysts, *Appl. Catal., A*, 2000, **196**, 1–8.

13 R. Koirala, O. V. Safonova, S. E. Pratsinis and A. Baiker, Effect of cobalt loading on structure and catalytic behavior of CoO_x/SiO_2 in CO_2-assisted dehydrogenation of ethane, *Appl. Catal., A*, 2018, **552**, 77–85, DOI: **10.1016/j.apcata.2017.12.025**.

14 S. Deng, H. Li, S. Li and Y. Zhang, Activity and characterization of modified Cr_2O_3/ZrO_2 nano-composite catalysts for oxidative dehydrogenation of ethane to ethylene with CO_2, *J. Mol. Catal. A: Chem.*, 2007, **268**(1–2), 169–175, DOI: **10.1016/j.molcata.2006.12.033**.

15 M. Numan, E. Eom, A. Li, M. Mazur, H. W. Cha, H. C. Ham, C. Jo and S.-E. Park, Oxidative Dehydrogenation of Ethane with CO_2 as a Soft Oxidant over a PtCe Bimetallic Catalyst, *ACS Catal.*, 2021, **11**(15), 9221–9232, DOI: **10.1021/acscatal.1c01156**.

16 N. Mimura, I. Takahara, M. Inaba, M. Okamoto and K. Murata, High-performance Cr/H-ZSM-5 catalysts for oxidative dehydrogenation of ethane to ethylene with CO_2 as an oxidant, *Catal. Commun.*, 2002, **3**(6), 257–262, DOI: **10.1016/s1566-7367(02)00117-6**.

17 M. Numan, T. Kim, C. Jo and S.-E. Park, Ethane Dehydrogenation with CO_2 as a soft oxidant over a Cr-TUD-1 catalyst, *J. CO2 Util.*, 2020, **39**, 101184, DOI: **10.1016/j.jcou.2020.101184**.

18 B. Yan, S. Yao, S. Kattel, Q. Wu, Z. Xie, E. Gomez, P. Liu, D. Su and J. G. Chen, Active sites for tandem reactions of CO_2 reduction and ethane dehydrogenation, *Proc. Natl. Acad. Sci. U. S. A.*, 2018, **115**(33), 8278–8283, DOI: **10.1073/pnas.1806950115**.

19 S. Deng, S.-G. Li, H.-Q. Li and Y. Zhang, Oxidative dehydrogenation of ethane to ethylene with CO_2 over Fe-$CrZrO_2$ catalysts, *Ind. Eng. Chem. Res.*, 2009, **48**, 7561–7566, DOI: **10.1021/ie9007387**.

20 V. Kocevski, G. Pilania and B. P. Uberuaga, High-throughput investigation of the formation of double spinels, *J. Mater. Chem. A*, 2020, **8**(48), 25756–25767, DOI: **10.1039/d0ta09200b**.

21 S. Bhandari, R. Khatun, T. S. Khan, D. Khurana, M. K. Poddar, A. Shukla, V. V. D. N. Prasad and R. Bal, Preparation of a nanostructured iron chromite spinel in the pure form and its catalytic activity for the selective oxidation of benzene to phenol: experimental and DFT

studies, *Green Chem.*, 2022, **24**(23), 9303–9314, DOI: **10.1039/d2gc02335k**.

22 I. I. Mishanin and V. I. Bogdan, *In situ* CO_2 reactivation of FeCrO/C catalyst in the oxidative dehydrogenation of ethane to ethylene, *Mendeleev Commun.*, 2020, **30**(3), 359–361, DOI: **10.1016/j.mencom.2020.05.033**.

23 I. I. Mishanin, T. V. Bogdan, A. E. Koklin and V. I. Bogdan, Design of highly selective heterogeneous catalyst for CO_2-mediated ethane oxidative dehydrogenation based on nonoxidative catalysis in stainless-steel reactor, *Chem. Eng. J.*, 2022, **446**, 137184, DOI: **10.1016/j.cej.2022.137184**.

24 I. I. Mishanin, T. V. Bogdan, A. V. Smirnov, P. A. Chernavskii, N. N. Kuznetsova and V. I. Bogdan, Formation of active phases of Fe/C, Cr/C and Fe–Cr/C catalysts in oxidative dehydrogenation of ethane, *Mendeleev Commun.*, 2023, **33**(3), 422–424, DOI: **10.1016/j.mencom.2023.04.039**.

25 O. A. Kim, T. V. Bogdan, A. E. Koklin and V. I. Bogdan, Interaction of Carbon Dioxide with Hydrogen on Supported Fe, Cr-Containing Catalysts, *Russ. J. Phys. Chem. B*, 2023, **16**(7), 1218–1220, DOI: **10.1134/s1990793122070107**.

26 T. V. Bogdan, A. E. Koklin, I. I. Mishanin, P. A. Chernavsky, D. A. Pankratov, O.-S. A. Kim and V. Bogdan, CO_2 Hydrogenation on Carbides Formed *in situ* on Carbon-Supported Iron-Based Catalysts in High-Density Supercritical Medium, *ChemPlusChem*, 2024, **89**, e202400327, DOI: **10.1002/cplu.202400327**.

27 B. Ravel and M. Newville, ATHENA, ARTEMIS, HEPHAESTUS: data analysis for X-ray absorption spectroscopy using IFEFFIT, *J. Synchrotron Radiat.*, 2005, **12**(4), 537–541, DOI: **10.1107/s0909049505012719**.

28 F. Cancino-Trejo, V. Santes, J. A. A. Cardenas, M. Gallardo, Y. G. Maldonado, L. Miranda A, O. Valdes, J. A. de los Reyes and C. E. Santolalla-Vargas, Active Ni and Fe species on catalysts Ni/Al_2O_3 and $NiFe/Al_2O_3$ for the oxidative dehydrogenation (ODH) of ethane to ethylene assisted by CO_2, *Chem. Eng. J. Adv.*, 2022, **12**, 100404, DOI: **10.1016/j.ceja.2022.100404**.

29 P. Liu, L. Zhang, X. Wang, M. Du, Y. Hao, L. Li, X. Chen, N. Sun and W. Wei, Preparation, Structure-Performance Relationship, and Reaction Network of ZnZSM-5 for Oxidative Dehydrogenation of Ethane with CO_2, *Chemistry*, 2023, **29**(22), e202203960, DOI: **10.1002/chem.202203960**.

30 S. Yao, B. Yan, Z. Jiang, Z. Liu, Q. Wu, J. H. Lee and J. G. Chen, Combining CO_2 Reduction with Ethane Oxidative Dehydrogenation by Oxygen-Modification of Molybdenum Carbide, *ACS Catal.*, 2018, **8**(6), 5374–5381, DOI: **10.1021/acscatal.8b00541**.

31 R. D. Shannon, Revised effective ionic radii and systematic studies of interatomic distances in halides and chalcogenides, *Acta Crystallogr., Sect. A*, 1976, **32**, 751–767, DOI: **10.1107/s0567739476001551**.

32 M. E. Montero-Cabrera, L. E. Fuentes-Cobas, E. Macías-Ríos and M. E. Fuentes-Montero, Application of X-ray absorption fine structure (XAFS) to local-order analysis in Fe-Cr maghemite-like materials, *AIP Conf. Proc.*, 2015, **1671**, 020008, DOI: **10.1063/1.4927185**.

33 M. García-Vázquez, K. Wang, J. M. González-Carballo, D. Brown, P. Landon, R. Tooze and F. R. García-García, Iron and chromium-based oxides for residual methane abatement under realistic conditions: a study on sulfur dioxide poisoning and steam-induced inhibition, *Appl. Catal., B*, 2020, **277**, 119139, DOI: **10.1016/j.apcatb.2020.119139**.

34 G. C. Chinchen, R. H. Logan and M. S. Spencer, Water-gas shift reaction over an iron oxide/chromium oxide catalyst, *Appl. Catal.*, 1984, **12**(1), 89–96, DOI: **10.1016/s0166-9834(00)81506-7**.

35 F. Meshkani, M. Rezaei and M. Jafarbegloo, Preparation of nanocrystalline Fe_2O_3–Cr_2O_3–CuO powder by a modified urea hydrolysis method: a highly active and stable catalyst for high temperature water gas shift reaction, *Mater. Res. Bull.*, 2015, **64**, 418–424, DOI: **10.1016/j.materresbull.2014.12.038**.

36 M. I. Baraton, G. Busca, M. C. Prieto, G. Ricchiardi and V. Sanchez Escribano, On the Vibrational Spectra and Structure of $FeCrO_3$ and of the Ilmenite-Type Compounds $CoTiO_3$ and $NiTiO_3$, *J. Solid State Chem.*, 1994, **112**(112), 9–14.

37 D. Renusch, B. Veal, K. Natesan and M. Grimsditch, Transient oxidation in Fe-Cr-Ni alloys A Raman-scattering study, *Oxid. Met.*, 1996, **46**, 365–381.

38 P. Bhardwaj, J. Singh, R. Kumar, D. Kumar, V. Verma and R. Kumar, Oxygen defects induced tailored optical and magnetic properties of $Fe_xCr_{2-x}O_{3(0\leq x\leq 0.1)}$ nanoparticles, *Appl. Phys. A: Mater. Sci. Process.*, 2022, **128**(2), 135, DOI: **10.1007/s00339-021-05233-x**.

39 H. K. Mehtani, M. I. Khan, B. N. Jaya, S. Parida, M. J. N. V. Prasad and I. Samajdar, The oxidation behavior of iron-chromium alloys: the defining role of substrate chemistry on kinetics, microstructure and mechanical properties of the oxide scale, *J. Alloys Compd.*, 2021, **871**, 159583, DOI: **10.1016/j.jallcom.2021.159583**.

40 I. Banerjee, H. K. D. Kim, D. Pisani, K. P. Mohanchandra and G. P. Carman, Magnetic anisotropy and magnetodielectric coefficients in Cr_2O_3 and $Fe_{0.4}Cr_{1.6}O_3$, *J. Alloys Compd.*, 2014, **614**, 305–309, DOI: **10.1016/j.jallcom.2014.06.038**.

41 L. Z. Liu, T. H. Li, X. L. Wu, J. C. Shen and P. K. Chu, Identification of oxygen vacancy types from Raman spectra of Sn_2 nanocrystals, *J. Raman Spectrosc.*, 2012, **43**(10), 1423–1426, DOI: **10.1002/jrs.4078**.

42 X. Yue, L. Zhang, L. Ma, M. Lu, A. Neville and Y. Hua, Influence of a small velocity variation on the evolution of the corrosion products and corrosion behaviour of super ^{13}Cr SS in a geothermal CO_2 containing environment, *Corros. Sci.*, 2021, **178**, 108983, DOI: **10.1016/j.corsci.2020.108983**.

43 H.-Y. Lin, Y.-W. Chen and C. Li, The mechanism of reduction of iron oxide by hydrogen, *Thermochim. Acta*, 2003, **400**(1–2), 61–67, DOI: **10.1016/s0040-6031(02)00478-1**.

44 V. V. Kovalenko, M. N. Rumyantseva, A. M. Gaskov, E. V. Makshina, V. V. Yushchenko, I. I. Ivanova, A. Ponzoni, G. Faglia and E. Comini, SnO_2/Fe_2O_3 nanocomposites: ethanol-sensing performance and

catalytic activity for oxidation of ethanol, *Inorg. Mater.*, 2006, **42**(10), 1088–1093, DOI: **10.1134/s0020168506100074**.

45 V. Galvita and K. Sundmacher, Redox behavior and reduction mechanism of Fe_2O_3–$CeZrO_2$ as oxygen storage material, *J. Mater. Sci.*, 2007, **42**(22), 9300–9307, DOI: **10.1007/s10853-007-1872-7**.

46 Y.-Q. Wang, Y.-X. Li, X. Fu, J.-Y. Yue, J.-W. Cao, X.-B. Ma, F. Liu and J.-W. Wang, Catalytic oxidation of toluene by binary metal oxide Cr_2O_3/CeO_2 from MIL-101 (Cr), *J. Solid State Chem.*, 2023, **328**, 124334, DOI: **10.1016/j.jssc.2023.124334**.

47 G. Festa, A. Serrano-Lotina, E. Meloni, R. Portela, C. Ruocco, M. Martino and V. Palma, Support Screening to Shape Propane Dehydrogenation SnPt-Based Catalysts, *Ind. Eng. Chem. Res.*, 2024, **63**, 16269–16284, DOI: **10.1021/acs.iecr.3c04089**.

48 J. Tian, P. Zheng, T. Zhang, Z. Han, W. Xu, F. Gu, F. Wang, Z. Zhang, Z. Zhong, F. Su, *et al.*, CO_2 methanation over Ni nanoparticles inversely loaded with CeO_2 and Cr_2O_3: catalytic functions of metal oxide/Ni interfaces, *Appl. Catal., B*, 2023, **339**, 123121, DOI: **10.1016/j.apcatb.2023.123121**.

49 Z. Xie, B. Yan, J. H. Lee, Q. Wu, X. Li, B. Zhao, D. Su, L. Zhang and J. G. Chen, Effects of oxide supports on the CO_2 reforming of ethane over Pt-Ni bimetallic catalysts, *Appl. Catal., B*, 2019, **245**, 376–388, DOI: **10.1016/j.apcatb.2018.12.070**.

50 V. Thapliyal, M. E. Alabdulkarim, D. R. Whelan, B. Mainali and J. L. Maxwell, A concise review of the Raman spectra of carbon allotropes, *Diamond Relat. Mater.*, 2022, **127**, 109180, DOI: **10.1016/j.diamond.2022.109180**.